Inorganic Chemistry

pubs.acs.org/IC

Forum Article

Complexes of Platinum Group Metals with a Conformationally Locked Scorpionate in a Metal−Organic Framework: An Unusually Close Apical Interaction of Palladium(II)

Michael T. Payne, Constanze N. Neumann, Eli Stavitski, and Mircea Dincă*

Cite This: https://doi.org/10.1021/acs.inorgchem.1c00941

Read Online

ACCESS | Metrics & More | Article Recommendations | Supporting Information

ABSTRACT: We report synthetic strategies for installing platinum group metals (PGMs: Pd, Rh, Ir, and Pt) on a scorpionate-derived linker (TpmC*) within a metal−organic framework (MOF), both by room-temperature postsynthetic metalation and by direct solvothermal synthesis, with a wide range of metal loadings relevant for fundamental studies and catalysis. In-depth studies for the palladium adduct Pd(II)@Zr-TpmC* by density-functional-theory-assisted extended X-ray absorption fine structure spectroscopy reveals that the rigid MOF lattice enforces a close Pd(II)−N_{apical} interaction between the bidentate palladium complex and the third uncoordinated pyrazole arm of the TpmC* ligand (Pd−N_{apical} = 2.501 ± 0.067 Å), an interaction that is wholly avoided in molecular palladium scorpionates.

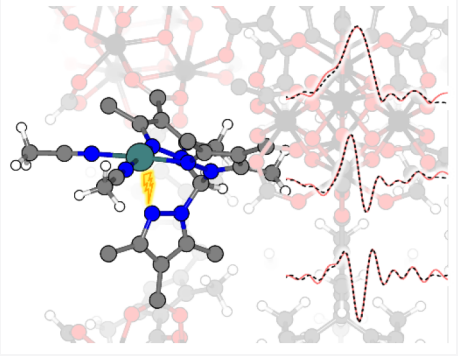

INTRODUCTION

The scorpionate ligands tris(pyrazolylborate) (Tp) and tris(pyrazolylmethane) (Tpm), introduced by Trofimenko in the late 1960s,[1] can tightly chelate a metal by facial κ^3 coordination while retaining open cis-oriented coordination sites. The resulting stable metal complexes are capable of concerted oxidative addition and reductive elimination. This has enabled fundamental studies of the properties of second- and third-row transition metals, exemplified by Canty's use of scorpionates to stabilize high-oxidation-state organometallic complexes of palladium and platinum,[2] as well as novel reactivity, such as the C−H activation chemistry of rhodium, iridium, and ruthenium scorpionates.[3]

The coordination chemistry of scorpionates, however, can be challenging to control in molecular systems: coordination sites required for catalysis are often blocked via intermolecular pathways such as homoleptic ML_2 complex formation and $(ML)_2$ dimerization (Figure 1a). Undesired intermolecular interactions are exacerbated by the rotational lability of the pyrazole rings, which allows the scorpionate to bridge multiple metals while also opening additional ligand degradation pathways via intramolecular C−H activation. These destructive pathways can be blocked by the installation of bulky substituents on the pyrazole rings,[4] but such ligands are often difficult to synthesize, and steric encumbrance of the active site limits both metal ligation and overall catalyst activity.

In principle, bimolecular deactivation or decomposition pathways can be eliminated altogether by immobilizing the ligand in a solid matrix, locking the conformation and position of the scorpionate. Metal−organic frameworks (MOFs) are privileged among solid-state materials because of their modular structure and molecular tunability, offering a capacity for design and optimization ideal for supporting well-defined metal complexes.[5] In the case of first-row transition metals, the heterogenization of scorpionate-based catalysts in the MOFs MFU-4l and CFA-1 led to long-lived catalysts that replicated the characteristic reactivity of their molecular analogues while eschewing bimolecular deactivation pathways.[6−12] The requisite catalytically active transition-metal centers were installed in the secondary building unit (SBU) by the cation exchange of structural metals, but the widespread success of this strategy for first-row transition metals has not translated to platinum group metals (PGMs: Pd, Rh, Ir, and Pt). To our knowledge, there is only one reported introduction of a second- or third-row transition metal containing a partially filled d shell into an SBU.[13]

Alternatively, single-site installation of a reactive metal onto the linker of a MOF produces a well-defined heterogeneous catalyst that can be studied and tuned with molecular precision.[14−16] Beyond the simple translation of homogeneous systems to solid supports, site isolation in a MOF can confer

Special Issue: Postsynthetic Modification of Metal-Organic Frameworks

Received: March 26, 2021

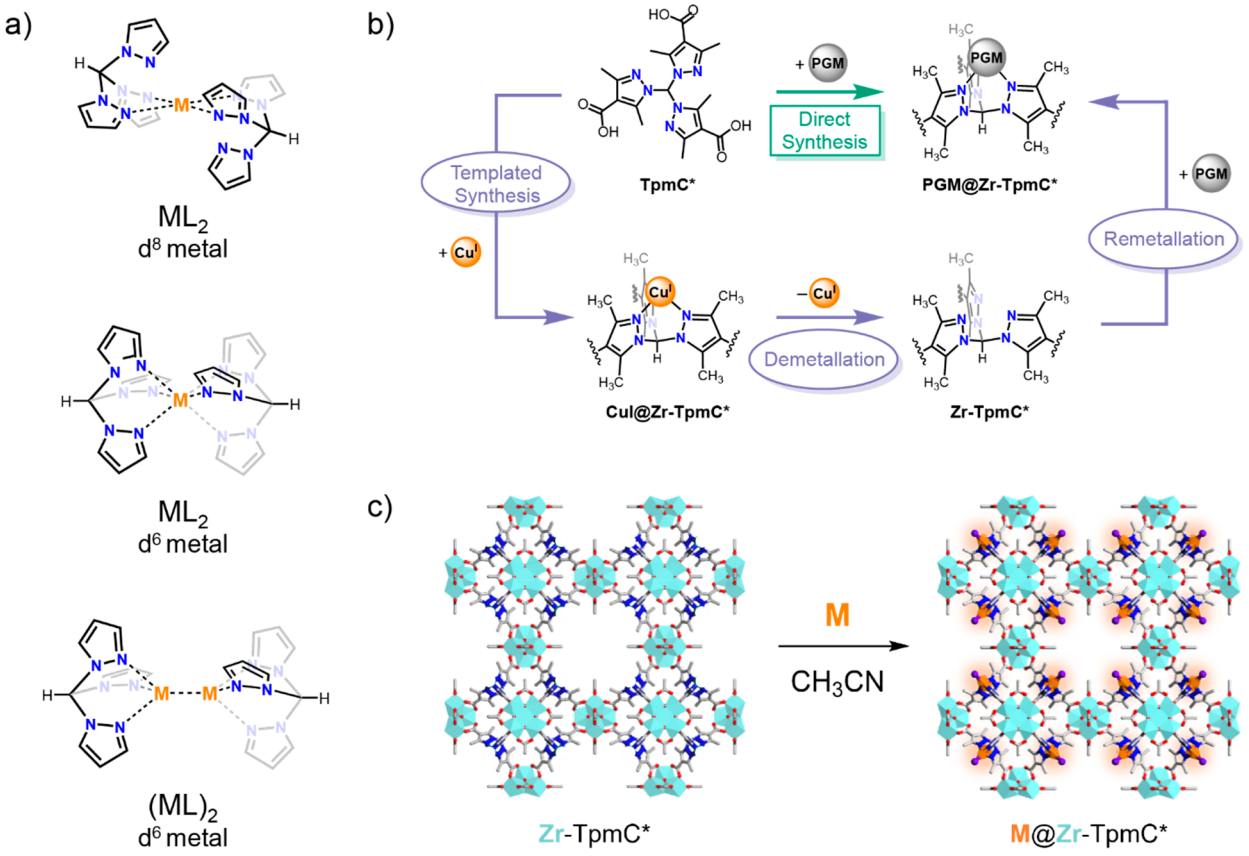

Figure 1. (a) Deactivation modes of molecular metal scorpionates by homoleptic ML_2 formation and $(ML)_2$ dimerization. (b) Synthetic routes for accessing site-isolated PGM scorpionates using the Zr-TpmC* MOF. (c) Generic scheme for remetalation of Zr-TpmC*.

new catalytic properties by modulating the catalyst microenvironment, restricting the ligand flexibility, and stabilizing against biomolecular decomposition;[17] thus, methodologies for producing new MOF-supported metal species offer the means to access new reactivity with existing catalysts. Recently, our group reported a MOF composed of a Tpm-based linker, $\{(TpmC^*)_8[Zr_6O_4(OH)_4(X)_4(H_2O)_4]_3\}$ (Zr-TpmC*; X = HO^- or $HCOO^-$).[18] Attempts at the direct solvothermal synthesis of Zr-TpmC* led to the exclusive formation of amorphous materials, which we attributed to the conformational flexibility of the free ligand. However, TpmC* could be templated in situ with rigid C_{3v} symmetry, required for the Zr-TpmC* framework, via metalation with CuI during MOF synthesis to produce crystalline CuI@Zr-TpmC*. Subsequent treatment of CuI@Zr-TpmC* with 1 M HCl removed templating equivalents of CuI to yield crystalline free-base Zr-TpmC* (Scheme S2). We hypothesized that free-base Zr-TpmC* would be capable of supporting PGM scorpionates without the need for SBU cation exchange. Indeed, we found that the free-base MOF could be readily metalated with suitable precursors to yield the corresponding palladium, rhodium, iridium, and platinum scorpionate complexes within a heterogeneous host (Figure 1b,c). PGM@Zr-TpmC* represents the first report of MOF-supported second- and third-row transition-metal scorpionates. Both high PGM loadings, ideal for mechanistic and structural studies, and low metal loadings that minimize mass-transfer limitations in catalytic applications could be accessed.

We further demonstrate that Ir@Zr-TpmC* and Rh@Zr-TpmC* are readily prepared not only by postsynthetic modification of free-base Zr-TpmC* but also by direct solvothermal synthesis of the MOF in the presence of $IrCl_3$ and $RhCl_3$, which coordinate to TpmC* and template the ligand with C_{3v} symmetry, thereby avoiding laborious copper templation and demetalation steps (vide supra). The two complementary synthetic pathways of postsynthetic metalation and direct synthesis provide access to a diverse suite of PGM@Zr-TpmC* systems (Figure 1b) and lay the foundation for the introduction of a wide range of elements into MOF-supported scorpionates. Detailed further investigation by X-ray absorption spectroscopy (XAS) and complementary density functional theory (DFT) calculations revealed that the MOF support can impart a unique PGM coordination environment that is distinct from the corresponding molecular complex, as was the case for the geometrically frustrated interaction of the TpmC* metalloligand with square-planar Pd(II). We observe that the rigid MOF lattice enforces an unusually short Pd(II)–N_{apical} interaction (2.501 Å), which we attribute to the metalloligand being conformationally locked in C_{3v} symmetry by the MOF framework. In molecular systems, short interatomic distances between square-planar Pd(II) centers and elements capable of acting as axial ligands are reported to lower the oxidation potential of Pd(II) and concomitantly stabilize the III+ and IV+ oxidation states.[19,20] The short Pd–N_{apical} interaction enforced by the MOF support and limited molecular motion required for the coordination of an axial ligand suggests that Pd(II)@Zr-TpmC* may display a low

https://doi.org/10.1021/acs.inorgchem.1c00941
Inorg. Chem. XXXX, XXX, XXX–XXX

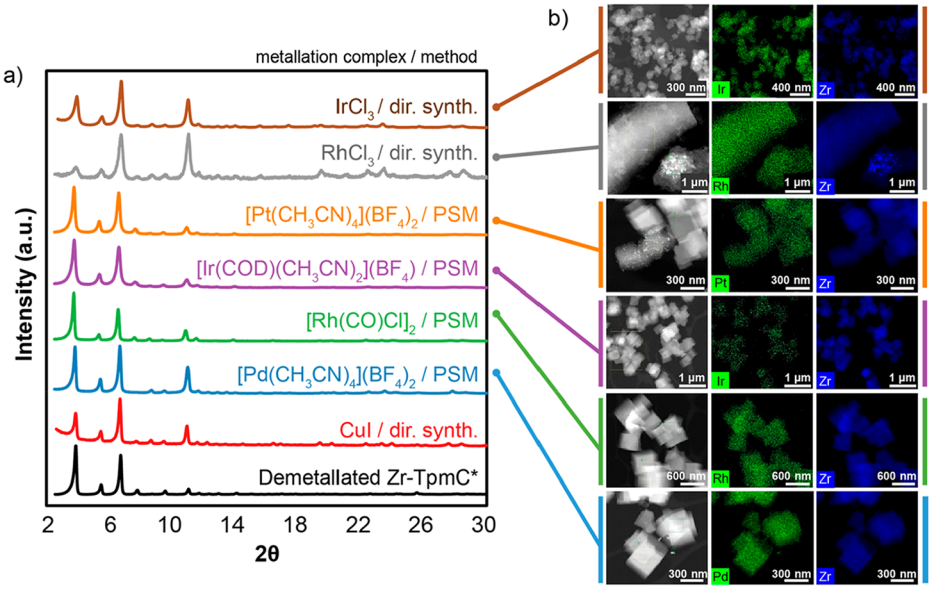

Figure 2. (a) PXRD patterns of PGM@Zr-TpmC*. (b) TEM/EDS images of PGM@Zr-TpmC*. PSM = postsynthetic metalation.

barrier for the oxidation of Pd, a desirable feature in high-valent Pd catalysis.

RESULTS AND DISCUSSION

Scorpionate Sites in Zr-TpmC* That Are Quantitatively Metalated by Pd(II) via Postsynthetic Modification. We first pursued the synthesis of a Pd(II)@Zr-TpmC* system using $[Pd(CH_3CN)_4](BF_4)_2$ as a Pd(II) source, based on the assumption that the labile acetonitrile (CH_3CN) ligands and weakly coordinating anions would facilitate PGM installation. Activated free-base Zr-TpmC* was soaked in an CH_3CN solution of $[Pd(CH_3CN)_4](BF_4)_2$ containing 1 equiv of Pd complex per 1 equiv of an open TpmC* binding site over a period of 5 days. During this time, the yellow-orange color of the solution faded and the MOF sample changed in color from white to yellow, suggesting that the Pd complex had been absorbed into the framework. The product was recovered, washed, and dried to yield a yellow microcrystalline powder, which we assign as $[Pd(CH_3CN)_2](BF_4)_2$@Zr-TpmC* (**1**). Characterization of **1** by powder X-ray diffraction (PXRD) shows that the crystallinity of Zr-TpmC* is maintained (Figure 2a) with no signature of Pd nanoparticle formation (Figure S9).

In our initial report on Zr-TpmC*, we observed that the remetalation of Zr-TpmC* by $[Cu(CH_3CN)_4](BF_4)$ plateaued at 4 equiv of Cu per formula unit (50% of the available TpmC* sites). In contrast, we achieved nearly complete metalation of Zr-TpmC* using $[Pd(CH_3CN)_4](BF_4)_2$, with up to 7 equiv of Pd installed per formula unit (vs eight available TpmC* sites), as determined by inductively coupled plasma mass spectrometry (ICP-MS). Furthermore, while cation exchange typically requires large excesses of metal for significant incorporation, metalation of Zr-TpmC* by Pd is nearly quantitative, with >80% Pd incorporation at a range of substoichiometric loadings (Figure S11). Such an efficient incorporation is essential when preparing catalysts from precious metals such as Pd, given their high costs. Reaction with an excess of $Pd(CH_3CN)_4(BF_4)_2$ does not increase the metal loading to exceed 7 equiv of Pd per formula unit, suggesting that excess Pd does not deposit elsewhere in the framework. Successful metalation of the TpmC* site (and the absence of Pd nanoparticles) is corroborated by transmission electron microscopy/energy-dispersive X-ray spectroscopy (TEM/EDS) imaging of **1**, which showed even incorporation of Pd throughout the Zr-TpmC* crystallites (Figure 2b).

Further experimental characterization of **1** provides evidence that the metalation reagent $Pd(CH_3CN)_4(BF_4)_2$ is ultimately incorporated at the scorpionate sites, losing two CH_3CN ligands to form $[Pd(CH_3CN)_2(TpmC^*)]^{2+}$ units, whose charge is balanced by BF_4^- presumably residing in the pores. A PXRD experiment gives direct evidence for the uniform introduction of Pd into the scorpionate site because the 7.8° peak, which corresponds to the (200) reflection, is observed to systematically decrease in intensity with increasing Pd loading (Figure 3a). We attribute this to a phase cancellation phenomenon caused by heavy atoms in the scorpionate sites, which lie directly between the (200) planes and thus diffract 180° out-of-phase with the (200) reflection (Figure S13). The CH_3CN ligands bound to Pd in **1** were also detected by IR spectroscopy as weak bands at 2310 and 2340 cm^{-1} (Figure 3b). These C≡N stretch bands are red-shifted by approximately 10 cm^{-1} in comparison with free $[Pd(CH_3CN)_4](BF_4)_2$. We ascribe the red shift to the exchange of two weakly π-accepting nitrile ligands for the framework pyrazole ligands, which would effectively behave only as σ donors due to a fixed orientation that gives poor d−π^* overlap (Figure 4b); back-bonding to the remaining nitrile ligands would thus increase, and the C−N triple bond would concomitantly weaken. Characterization of **1** digested in D_2SO_4/deuterated dimethyl sulfoxide (DMSO-d_6) by ^{19}F NMR spectroscopy confirmed the presence of BF_4^- as the charge-compensating anion (Figure S8). Although CH_3CN was detected by IR, no CH_3CN was observed in the ^1H NMR spectrum of digested **1**. We hypothesize that strong acid and trace water in the digestion conditions may induce hydrolysis of CH_3CN to acetic acid, as the latter was observed in the ^1H NMR spectrum (Figure S7).[21]

The successful incorporation of Pd at the TpmC* scorpionate site in **1** is further evidenced by the X-ray photoelectron spectroscopy (XPS) data, which shows an

https://doi.org/10.1021/acs.inorgchem.1c00941
Inorg. Chem. XXXX, XXX, XXX−XXX

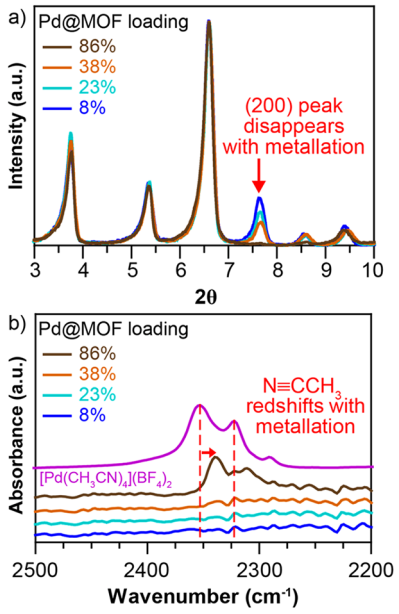

Figure 3. (a) PXRD overlay of Zr-TpmC* samples with various Pd loadings (percentage is versus the total accessible TpmC* ligand). (b) IR spectrum overlay of Zr-TpmC* samples with various Pd loadings. The Pd loading was determined as the Pd content versus the available TpmC* sites by ICP-MS.

increase of 0.2−0.3 eV in the N 1s binding energy associated with the scorpionate pyrazoles upon metalation and a concomitant decrease of more than 1 eV in the Pd $3d_{5/2}$ binding energy compared with $[Pd(CH_3CN)_4](BF_4)_2$ (Table S2). The observed Pd $3d_{5/2}$ binding energy is consistent with the assignment of the Pd oxidation state in **1** as II+, an assignment that is also supported by solid-state XAS measurements of **1** collected at the Pd K-edge (24350 eV) (Figure S10). Qualitative comparisons of the X-ray absorption near-edge structure (XANES) with reference Pd compounds are also consistent with a II+ oxidation state and reflect a decrease in the Pd binding energy.

DFT-Assisted Extended X-ray Absorption Fine Structure Spectroscopy (EXAFS) Characterization of Pd(II)@Zr-TpmC* That Reveals an Unusually Close Pd−N Apical Interaction. In addition to a confirmation of the metal oxidation state, an XAS study of Pd@Zr-TmpC* was pursued to shed light on the coordination environment of Pd(II), a d^8 metal with a strong electronic preference for square-planar geometry, placed in the scorpionate binding site of **2**, which is conformationally locked in C_{3v} symmetry by the MOF lattice (Figure 4a). In molecular palladium(II) scorpionates, the tridentate ligand is coordinated via two of the three pyrazoles in an edge-on κ^2 fashion, with the third pyrazole donor rotated 90° to avoid an unfavorable filled−filled interaction with the Pd d_{z^2} orbital.[2,22] Upon two-electron oxidation of Pd(II) to Pd(IV) d^6, the electronic preference shifts to favor an octahedral geometry, allowing the formation of stable κ^3-scorpionate complexes. Because rotation of the pyrazoles in Zr-TpmC* is inhibited by carboxylate linkages to the SBU, we hypothesized that this rigidity would enforce an unusually close apical interaction between the palladium(II) κ^2-scorpionate and the third pyrazole arm of the ligand. Such an interaction could promote oxidation to a Pd(IV) complex by preconfiguring the Pd for an octahedral geometry.

To directly probe the local coordination environment of Pd in **1**, we employed DFT-assisted EXAFS analysis, an established technique for understanding the local structure of metal atoms in MOFs as well as zeolites, organometallic complexes, and inorganic salts.[23] The initial cluster model used for EXAFS fitting was based on the crystallographic data of CuI@Zr-TpmC*,[18] $Pd(Tpm)_2(BF_4)_2$, and $Pd(CH_3CN)_4(BF_4)_2$,[24] and the model was structurally optimized

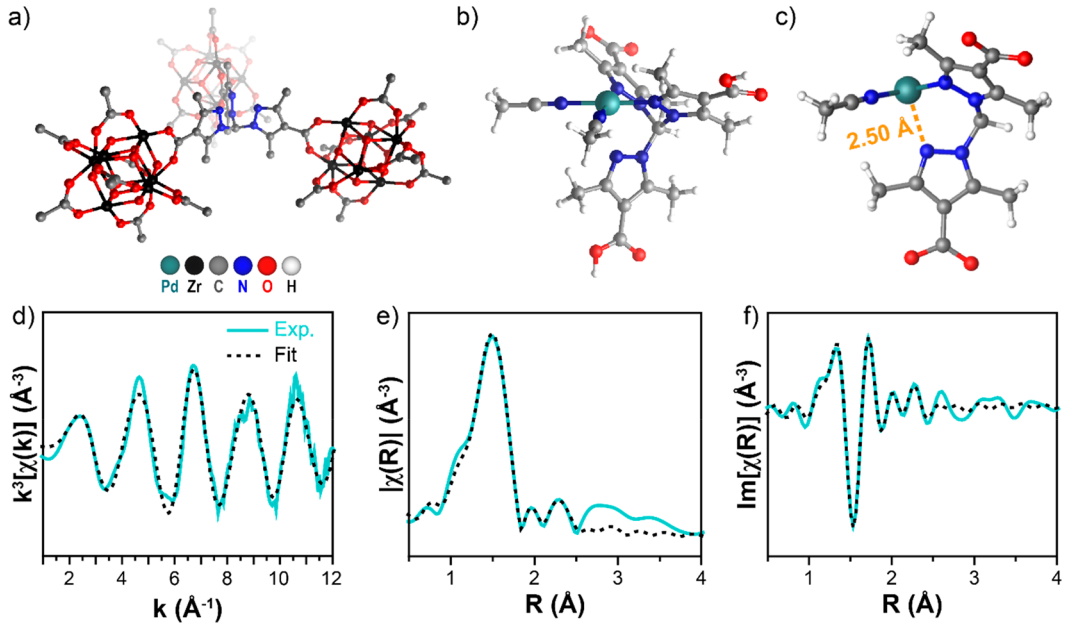

Figure 4. (a) Coordination of TpmC* to Zr-oxo nodes in **1** (protons omitted for visual clarity). (b) Optimized DFT model of the $[Pd(CH_3CN)_2TpmC^*]^{2+}$ fragment used for EXAFS fitting. (c) Close Pd−N_{apical} interaction in **2**, determined by EXAFS fitting. (d) k^3-weighted EXAFS signal and corresponding modulus (e) and imaginary (f) parts of the phase-uncorrected FT of the experimental and best fits for $[Pd(CH_3CN)_2TpmC^*]^{2+}$.

https://doi.org/10.1021/acs.inorgchem.1c00941
Inorg. Chem. XXXX, XXX, XXX−XXX

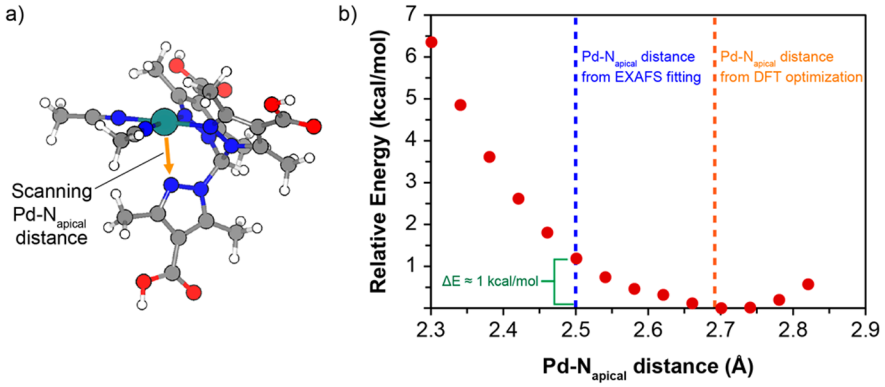

Figure 5. (a) Example structure for $[Pd(CH_3CN)_2(TpmC^*)]^{2+}$ highlighting the Pd−N_{apical} bond. (b) Relative energy (kcal/mol) versus Pd−N_{apical} distance (Å). A shallow PES surface is observed, which is within the error of DFT calculations.

using DFT (Figure 4a,b). During geometry optimization, the position of the carboxylic acid was kept fixed to account for the rigidity of the solid structure; analogous protocols have been employed for structure optimization of SBUs in several MOFs.[25−27] Optimized structures that did not include this restraint gave one imaginary frequency involving rotation of the apical pyrazole away from Pd, consistent with the previously mentioned behavior of molecular palladium(II) scorpionate systems (Figure S39).

The signal/noise ratio of the collected EXAFS data allowed us to fit single scattering (SS) paths from both the first and second coordination shells in the *R*-space interval ΔR = 1.0−3.1 Å. The first coordination shell consists of two acetonitrile N atoms and two pyrazole N atoms in square-planar geometry, which were modeled as an averaged four-atom shell of SS paths (N_1) with a single ΔR and Debye−Waller (σ^2) parameter. The second coordination shell consists of the apical imine N atom of the third pyrazole arm (N_{apical}) and the amine N atoms of the two coordinated pyrazoles (N_2). The obtained fit reproduces our experimental data well (Figure 4c−f), giving Pd−N_1 and Pd−N_2 bond distances that are in good agreement with both the DFT calculations and crystallographic data of analogous Pd compounds (Table S7). The EXAFS fitting revealed an unusually short Pd−N_{apical} distance of 2.501 ± 0.067 Å (Figure 4c) compared with other square-planar Pd(II) complexes. In the analogous molecular complex, a 90° rotation of the apical pyrazolate to both avoid the short Pd−N_{apical} distance and minimize steric interactions between adjacent pyrazolates would be expected, and such a rotation is observed in the reported crystal structures of palladium(II) scorpionates.[2,22,28−30] In contrast, the close Pd−N_{apical} distance is preserved in **1** by the rigid Tmp* binding pocket enforced by the MOF.

Further DFT calculations support the experimentally determined Pd−N_{apical} interatomic separation. Although the original DFT-optimized model predicted a Pd−N_{apical} distance that was approximately 0.2 Å longer than that determined by EXAFS fitting, a subsequent DFT structure optimization in which the Pd−N_{apical} distance was constrained to 2.501 Å raised the structure energy by less than 1 kcal/mol, a marginal increase that falls within the error of DFT calculations. Additionally, we conducted a relaxed potential energy surface (PES) scan, in which geometry optimization occurs at each step prior to energy calculation, across the Pd−N_{apical} bond distances R_{Pd-N} = 2.301−2.801 Å in 0.04 Å steps at the M06/SDD-6-311G(d,p) level of theory (Figure 5). The calculation revealed a shallow PES between the Pd−N_{apical} distances from EXAFS fitting and DFT optimization, indicating that the experimental data are compatible with calculations.

We thus draw a comparison to molecular complexes of Pd(II) with tetradentate diazapyridinophane ligands reported by Mirica et al., where the shortest Pd(II)−N_{apical} distance from X-ray crystal structures (2.525 Å) is slightly longer than the Pd(II)−N_{apical} distance that we observed in **1**.[19,20] The close Pd−N_{apical} interaction in the Mirica systems is reported to lower the oxidation potential of Pd and stabilize Pd in the III+ and IV+ oxidation states, and given the structural similarities, an analogous effect may be present in **1**. High-valent Pd systems find application in catalysis, enabling unprecedented organic transformations not accessible with conventional Pd(0)/Pd(II) systems.[31,32] Yet, to our knowledge, no well-defined Pd(III) or Pd(IV) species have been reported on a solid support, although transient Pd(III) or Pd(IV) has been proposed in the solid-state fluorination catalysis of Pd-functionalized metal−organic layers.[33] Our study of **1** suggests that the immobilization of ligands in a MOF in a geometry that preferentially stabilizes Pd(IV) over Pd(II) may be a viable strategy for the development of heterogeneous high-valent Pd catalysts.

Postsynthetic Installation of Rh, Pt, and Ir in Zr-TpmC*. Inspired by the successful synthesis of the MOF-based palladium scorpionate **1**, we pursued the metalation of Zr-TpmC* by other PGMs. We prioritized metalation precursors that have slim steric profiles to allow for facile mass transport into the MOF pores and/or labile ligands that are easily displaced by the framework-bound scorpionate. On the basis of these criteria, we chose the metalation precursor $[Rh(CO)_2Cl]_2$ for Rh, used to generate scorpionate catalysts for C−H bond activation,[3,34,35] and precursors $[Ir(CH_3CN)_2(COD)](BF_4)$ and $[Pt(CH_3CN)_4](BF_4)_2$ for Ir and Pt, respectively. When Zr-TpmC* was soaked in an CH_3CN solution of $[RhCl(CO)_2]_2$ over 4 days, the MOF sample turned bright yellow to form a product assigned as $[RhCl(CO)_2]$@Zr-TpmC* (**2**). Samples of **2** were prepared with varying amounts of Rh (0.1−2.0 equiv/TpmC* site). In contrast to metalation by $[Pd(CH_3CN)_4](BF_4)_2$, the color of the Rh solution did not completely fade, even when substoichiometric quantities of Rh were employed. Correspondingly, metalation of Zr-TpmC* by Rh was not quantitative, with a maximum of 0.4 Rh/TpmC* site installed in **2** (Figure S12). The surface area of Zr-TpmC* also decreases substantially upon metalation by $[Rh(CO)_2Cl]_2$,

https://doi.org/10.1021/acs.inorgchem.1c00941
Inorg. Chem. XXXX, XXX, XXX−XXX

from 1768 ± 40 m^2/g (Zr-TpmC*) to 701 ± 1 m^2/g (**2**, 0.4 Rh/TpmC* site). When characterized by PXRD, the intensity of the (200) reflection at 7.8° did not vary with Rh loading, but increasing Rh loading correlated with a pronounced increase in the intensity of the (100) reflection at 3.8° (Figure 6a). Given

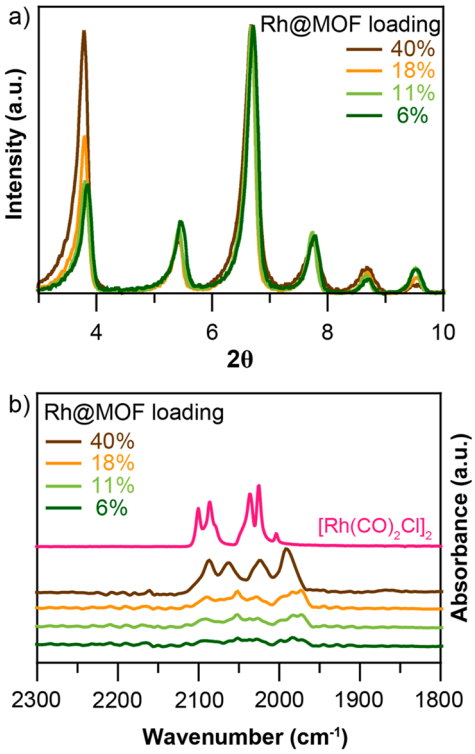

Figure 6. (a) PXRD overlay of Zr-TpmC* samples with varied Rh loading (percentage is vs the total accessible TpmC* ligand). (b) FTIR spectrum overlay of Zr-TpmC* samples with varied Rh loading versus metalation precursor $[Rh(CO)_2Cl]_2$. The Rh loading was determined as the Rh content versus the available TpmC* sites by ICP-MS.

that the intensities of low-angle reflections in the PXRD of MOFs are highly sensistive to disordered species such as the solvent in the pores,[36] the increasing intensity of the (100) reflection for increasing Rh loading in **2** suggests that $[Rh(CO)_2Cl]_2$ is encapsulated in the pores rather than incorporated into the TpmC* site. The small but systematic shift of the reflections to lower angles with increasing Rh loading could also be consistent with the pore filling, which can subtly distort the MOF structure and increase the size of the unit cell; however, we note that the PXRD patterns in Figure 6a were not referenced to an external standard and the samples were dried at room temperature (and thus not fully desolvated), so there is a minor experimental variance in the peak position from sample to sample.

To better interrogate the Rh speciation in **2**, Fourier transform infrared (FTIR) spectra were collected for both metalated Rh@MOF samples and the $[Rh(CO)_2Cl]_2$ metalation precursor (Figure 6b). The IR spectrum of $[Rh(CO)_2Cl]_2$ predominantly consists of four strong vibrations related to the carbonyl groups, namely, A_1 (2100 cm^{-1}), B_2 (2086 cm^{-1}), B_1 (2037 cm^{-1}), and A_2 (2025 cm^{-1}).[37] While the carbonyl vibrations are too weak to resolve for samples of **2** at lower loading, the sample of **2** at 40% loading (equivalents of Rh vs equivalents of the TpmC* sites) displays four clear vibrations at 2087, 2064, 2023, and 1992 cm^{-1}. We hypothesize that these four vibrations correspond to the four vibrations of the dimeric $[Rh(CO)_2Cl]_2$ metalation precursor and thus that $[Rh(CO)_2Cl]_2$ maintains its dimeric structure upon incorporation into the MOF. If the TpmC* sites were metalated by $[Rh(CO)_2Cl]_2$, the dimer would be expected to break, as is the case for molecular TpmC* complexes. In total, the PXRD, surface area, and FTIR analyses suggest that attempts to generate supported rhodium scorpionates in Zr-TpmC* with $[Rh(CO)_2Cl]_2$ instead deposit the Rh dimer intact within the pores.

Metalation of Zr-TpmC* with the third-row PGMs Ir and Pt was accomplished under conditions analogous to those of Pd and Rh to yield $[Ir(COD)BF_4]$@Zr-TpmC* (**3**, $x \approx 0-1.5$) and $[Pt(CH_3CN)_2(BF_4)_2]_x$@Zr-TpmC* (**4**, $x \approx 0-0.5$). As with Pd and Rh, the crystallinity of the MOF is retained and incorporation occurs evenly throughout the material, as determined by PXRD and TEM/EDS, respectively (Figure 1b). However, incorporation of the third-row metals Ir and Pt was substantially lower than that of the second-row metals, with a maximum of 0.19 Ir/TpmC* site in **3** and a maximum of 0.063 Pt/TpmC* site in **4**. Characterization of **3** and **4** by IR showed no discernible features of the molecular complex, a possible consequence of the low metal loadings.

Direct Synthesis That Provides an Alternative Route to Access PGM@Zr-TpmC*. Motivated to find synthetic routes that would result in higher metal incorporation for Rh, Ir, and Pt, we hypothesized that TpmC* could be templated in situ by metals other than Cu for direct MOF synthesis. Anticipating that a d^6 metal would provide the proper geometry for MOF synthesis, we attempted direct synthesis using $IrCl_3$. Indeed, the reaction of TpmC* with $IrCl_3$, $ZrOCl_2$, and benzoic acid in *N*,*N*-dimethylformamide (DMF) at 120 °C over 5 days yields off-white microcrystalline solids whose PXRD patterns match Zr-TpmC* and display no signatures of nanoparticle formation. We assigned these as $IrCl_3$@Zr-TpmC* (**5**) based on ICP-MS data, which gives a metal loading of 7.1 equiv of Ir per formula unit, equivalent to the full metalation achieved postsynthetically with $Pd(CH_3CN)_4(BF_4)_2$.

The Rh analogue, $RhCl_3$@Zr-TpmC* (**6**), can be similarly prepared by the direct synthesis of Zr-TpmC* in the presence of $RhCl_3$ (Figure S15). In some preparations, reaction temperatures above 60 °C resulted in blackened material, but no signature of Rh nanoparticles was visible in the powder diffractograms for these samples. The visible blackening of the solids, however, suggests that there may still be nanoparticles present in the sample that are too small to detect by PXRD. Characterization of **6** by TEM/EDS reveals an irregular crystallite morphology in contrast to the cubic crystallites of Zr-TpmC* and the PGM-metalated MOF samples (Figure 1b). Rh loading in these samples is also subquantitative, with 3.5 equiv of Rh per formula unit installed compared to the theoretical maximum of 8.

Attempts at the direct synthesis of Pd@Zr-TpmC* with the Pd(II) precursor Na_2PdCl_4 yielded only Pd nanoparticles, with analogous results for the Pt(II) precursor K_2PtCl_4. We attribute this outcome to two factors. First, the high temperature, acidic conditions, and trace water in the MOF synthesis can decompose DMF to produce amines that readily reduce Pd(II) and Pt(II), leading to the rapid formation and aggregation of Pd^0 and Pt^0 nanoparticles. Second, because of the strong electronic preference of d^8 metals for square-planar

https://doi.org/10.1021/acs.inorgchem.1c00941
Inorg. Chem. XXXX, XXX, XXX−XXX

geometry, coordination of Pd(II) and Pt(II) with TpmC* renders the C_{3v} geometry of the ligand higher in energy during synthesis, inhibiting formation of the Zr-TpmC* lattice. Preliminary attempts to access Pt@Zr-TpmC* by direct synthesis using the Pt(IV) precursor K_2PtCl_6 yielded gray solids whose PXRD pattern consists of broad peaks that correspond to the Zr-TpmC* structure (Figure S16), but similarly to the Rh direct synthesis, the reaction temperature and time were limited by Pt reduction and aggregation. Fortunately, postsynthetic modification avoids the reducing conditions of the MOF synthesis and thus allows for Pd/Pt incorporation into the scorpionate framework without the loss of metal to nanoparticle formation.

CONCLUSION

In summary, this work establishes synthetic methodologies for the installation of Pd, Rh, Ir, and Pt into the scorpionate sites of a MOF, while maintaining crystallinity and porosity. We further report the geometrically frustrated interaction between Pd(II) and a scorpionate ligand conformationally locked in C_{3v} symmetry by the MOF superstructure, as explored by DFT-assisted EXAFS analysis. An unusually close 2.5 Å Pd(II)–N_{apical} distance was observed that preconfigures the Pd for octahedral geometry and may lower its oxidation potential; a further study of the Pd@Zr-TpmC* systems may enable access to supported palladium scorpionates in higher oxidation states. Thus, this work not only extends the existing and well-defined chemistry of PGM scorpionates to MOFs but also signals emergent properties in such systems that can be probed and tuned with high fidelity thanks to the exceptional structural uniformity of MOFs.

EXPERIMENTAL METHODS

Reagents. $ZrOCl_2{\cdot}8H_2O$ and $[Pd(CH_3CN)_4](BF_4)_2$ were purchased from Alfa Aesar. CuI, $AgBF_4$, Na_2PdCl_4, $[Rh(CO)_2Cl]_2$, $RhCl_3$ hydrate, $IrCl_3$ hydrate, $[Ir(1,5\text{-COD})Cl]_2$, $PtCl_2$, K_2PtCl_4, and K_2PtCl_6 were purchased from Sigma-Aldrich. Ethyl diacetoacetate was purchased from TCI. *N*,*N*-Dimethylformamide (DMF), benzonitrile, acetonitrile (CH_3CN), acetone, ethanol, and chloroform were used as received without further purification. Ethyl 3,5-dimethylpyrazole-4-carboxylate was synthesized according to a reported procedure.[38] The MOF linker TpmC* was prepared following a previously reported procedure.[18]

Dry, deaerated CH_3CN and dichloromethane (DCM) were obtained by passing the solvent through two silica columns in a Glass Contour Solvent System and degassing with a flow of Ar gas for 30 min, followed by three freeze–pump–thaw cycles. All other commercial reagents were used as received without further purification.

General Procedures. *ICP-MS.* ICP-MS analyses were conducted at the MIT Center for Environmental Health Sciences (CEHS) using an Agilent 7900 ICP-MS spectrometer. Calibration standards were prepared for ICP-MS analysis using analytical standard solutions purchased from Ricca Chemicals and a 2% HNO_3 solution (prepared from EMD Millipore Omnitrace HNO_3 and ultrafiltered water). Digestion of PGM-containing samples was performed in aqua regia (HCl + HNO_3, Omni*Trace* Ultra, EMD Millipore) to ensure digestion of any metallic PGM.

IR Spectroscopy. Benchtop IR spectra were recorded on a Bruker Tensor 37 instrument with either a Ge or a diamond attenuated-total-reflectance sample holder.

PXRD. Laboratory PXRD patterns were collected on a Bruker D8 diffractometer fitted with a Goebel mirror and a Lynxeye Si-strip position-sensitive detector, operating in reflection mode with Ni-filtered Cu $K\alpha_{1,2}$ radiation ($K\alpha_1$ = 1.5406 Å, $K\alpha_2$ = 1.5444 Å, and $K\alpha_2/K\alpha_1$ = 0.5). The tube voltage and current were 40 kV and 40 mA, respectively. Samples for PXRD were prepared by placing a thin layer of the appropriate material on a zero-background Si crystal plate.

N_2 Adsorption Measurements. N_2 adsorption isotherms were measured by a volumetric method using a Micromeritics ASAP 2020 Plus gas sorption analyzer. Samples were activated at 110 °C (for demetalated Zr-TpmC* samples) or 95 °C (for metalated Zr-TpmC* samples) under high dynamic vacuum ($<10^{-4}$ mbar) for 18 h before analysis. All N analyses were performed using a liquid-nitrogen bath at 77 K. Oil-free vacuum pumps were used to prevent contamination of the sample or feed gases. Fits to the Brunauer–Emmett–Teller[39] equation satisfied the published consistency criteria.[40]

NMR. ^1H, ^{13}C, and ^{19}F NMR spectra were measured on a JEOL JNM-ECZ500R/S1 spectrometer (500 MHz).

XPS. XPS was conducted at Dow Chemical on a PHI VersaProbe II spectrometer equipped with an Al source using a 100 μm X-ray spot size. Samples were mounted using double-sided Cu tape. The charge shift was calibrated by setting either the hydrocarbon C 1s to 285.0 eV or the Si 2p of SiO_2 to 103.7 eV. Each point of the analysis was energy-corrected independently of the others.

Scanning Tunneling Electron Microscopy (STEM)/EDS. STEM/EDS analysis was conducted at Dow Chemical. Samples for TEM were prepared by mixing a small amount of sample powder with methanol. The fines were collected onto a standard Cu mesh TEM grid with a lacy C support. Data collection was performed using a FEI Themis field-emission-gun aberration-corrected (probe) transmission electron microscope. The microscope was operated at an accelerating voltage 200 keV. STEM images were collected at 2048 × 2048 image size. The Themis microscope has Bruker AXS XFlash EDS detectors with an energy resolution of 137 eV/channel for elemental identification and quantitative analysis. Instrument conditions: STEM 55–100 pA 70 μm C2 Spot 9 for imaging; ~300–500 pA for EDS map collection; 700–1500 s collection time per map; 1024 × 1024 map size.

XAS. XAS measurements in the solid state were carried out at the Inner Shell Spectroscopy (ISS) beamline of the NSLS-II at BNL (Upton, NY). Data were collected at the Pd K-edge (24350 eV) using fluorescence detection with a passivated implanted planar silicon detector. Pellets of 5 mm diameter were pressed from a Pd-$(CH_3CN)_2(BF_4)_2$@Zr-TpmC* MOF and poly(ethylene glycol) (50:50 ratio by mass).

XAS data reduction and EXAFS extraction procedures were performed using the *Athena* code, while EXAFS analysis was done with the *Artemis* software from the *Demeter* package.[41] Once extracted, the k^3-weighted $\Delta(k)$ functions were Fourier-transformed in the *k*-space interval Δk = 2.0–12.0 Å^{-1} and fitted in the *R* space in the interval ΔR = 1.0–3.1 Å, potentially resulting in 13 independent parameters ($2\Delta k\Delta R/\pi > 13$; Table S6). The phases and amplitudes were calculated by the *FEFF6* code,[42] implemented in the *Artemis* software, using the DFT-optimized structures.

The first coordination shell of Pd consists of two CH_3CN N atoms and two pyrazole N atoms in square-planar geometry and was modeled as an averaged four-atom shell of SS paths with a single ΔR and Debye–Waller (σ^2) parameter because of the close similarity in the bond lengths. The SS paths involving N atoms in the second coordination shell were modeled using two sets of ΔR and σ^2 parameters: one for the two interior N atoms of the coordinated pyrazole rings and one for the apical N atom of the uncoordinated pyrazole ring.

Synthesis. *Triethyl 1,1′,1″-Methanetriyltris(3,5-dimethyl-1H-pyrazole-4-carboxylate) (TpmC*-Et).* To a 2 L round-bottomed flask containing ethyl 3,5-dimethylpyrazole-4-carboxylate (50.0 g, 297 mmol, 1 equiv) and $NBu_4^+Br^-$ (9.60 g, 29.8 mmol, 0.1 equiv) was added deionized water (320 mL). Sodium carbonate (157 g, 1.48 mol, 5 equiv) was added to the flask in portions. After all of the sodium carbonate was added, chloroform (360 mL) was added to the flask, and the reaction mixture was heated to reflux for 3 days. After the reaction mixture cooled to room temperature, toluene (400 mL) was added to the flask, and the mixture was filtered. The organic phase was collected via a separatory funnel, and the aqueous phase was then extracted with toluene (200 mL) three times. The combined organic

https://doi.org/10.1021/acs.inorgchem.1c00941
Inorg. Chem. XXXX, XXX, XXX–XXX

phases were dried over magnesium sulfate and concentrated to a minimum volume in vacuo, after which methanol (ca. 10 mL) was added to induce precipitation of the product. The flask was stored at 4 °C overnight and filtered the following day to recover brown solids. The crude product was washed by sonication in cold methanol (50 mL) and then filtered and dried in air to afford TpmC*-Et as a white powder. Yield: 18.8 g (36.8%). ^{1}H NMR (500 MHz, C_6D_6): δ 8.17 (s, 1H), 4.02 (q, J = 7.1 Hz, 6H), 2.42 (s, 9H), 2.36 (s, 9H), 0.93 (t, J = 7.1 Hz, 9H). ^{13}C NMR (126 MHz, C_6D_6): δ 163.40, 151.16, 145.98, 112.49, 80.86, 59.42, 14.46, 13.88, 10.57.

1,1′,1″-Methanetriyltris(3,5-dimethyl-1H-pyrazole-4-carboxylic acid) (TpmC).* In a 1 L round-bottomed flask, Na metal (19.0 g) was dissolved in ethanol (470 mL) stepwise by fully dissolving small pieces of Na (ca. 0.5 g) one at a time. ***Caution!****It is important to perform this step slowly and with caution to avoid overheating. Na is highly reactive and poses fire/explosion hazards, and the dissolution of Na in alcohol is exothermic and produces flammable hydrogen gas.* After complete dissolution of all Na, TpmC*-Et (9.18 g, 17.8 mmol) and deionized water (9.40 mL) were added to the solution. The reaction mixture was then heated to reflux for 30 min, during which the reaction mixture first cleared up and then became turbid again. After the reaction mixture cooled to room temperature, the solid was separated by filtration and redissolved in a minimal amount of deionized water. The mixture was acidified with glacial acetic acid (7.1 mL) and stored at 4 °C overnight. The product TpmC* was isolated by filtration and dried in air overnight to give a white powder. Yield: 6.52 g (84.9%). ^{1}H NMR (500 MHz, methanol-d_4): δ 8.49 (s, 1H), 2.38 (m, 18H). ^{13}C NMR (126 MHz, methanol-d_4): δ 167.10, 152.98, 147.87, 113.26, 80.85, 14.46, 10.89.

[CuI(TpmC)$_8$][Zr$_6$O$_4$(OH)$_4$(C$_6$H$_5$COO)$_4$]$_3$ (CuI@Zr-TpmC*).* In a 1 L glass bottle, TpmC* (1.49 g) and benzoic acid (74.0 g, 175 equiv) were sonicated in DMF (500 mL) until dissolved to form a colorless solution. Separately, copper(I) iodide (2.7 g, 4.0 equiv) and $ZrOCl_2 \cdot 8H_2O$ (2.79 g, 2.50 equiv) were dissolved in DMF (100 mL) in a 250 mL glass beaker. The two solutions were then combined in the 1 L glass bottle, which was capped and placed in an oven preheated to 120 °C for 4 days. After cooling to room temperature, the reaction mixture was filtered through a fine glass frit, collecting fine white solids. The solids were washed on the frit three times with DMF (100 mL) and dried on the frit to give a white powder, which was taken directly to the next step. Yield: 3.57 g of crude product. In the original published procedure,[18] the reaction mixture was heated to 120 °C for only 2 days, but we found that extending this reaction time tended to improve the crystallinity of the product. This procedure, however, still yielded only a microcrystalline product with reaction times as long as 11 days.

[Zr$_6$O$_4$(OH)$_4$(C$_6$H$_5$COO)$_4$]$_3$ (Zr-TpmC).* In a 1 L glass bottle, 3.57 g of as-synthesized Zr-TpmC* was suspended in a mixture of DMF (350 mL) and 4 M HCl (15 mL). With the bottle capped, the mixture was heated in an oven at 100 °C for 18 h. After the bottle cooled to room temperature, the solution was decanted. The acid treatment was repeated three more times, and then the demetalated MOF was isolated by filtration. The solids were washed by soaking in DMF (50 mL) for 4 h, with the solvent decanted and replaced each hour, and then the solids were transferred to a 20 mL vial and soaked in DMF overnight. The following day, the solvent was decanted and the solids were soaked in acetone (20 mL) for 4 h, with the solvent decanted and replaced every hour. The MOF was then activated under a dynamic vacuum at 110 °C for 18 h to give a white powder. Yield: 1.204 g (47% vs TpmC*); Cu:Zr = 0.001:1.000 as determined by ICP-MS.

[Ir(1,5-COD)(CH$_3$CN)$_2$]BF$_4$. The Ir(I) metalation complex was prepared by following a literature procedure.[43] In a N_2 glovebox, $[Ir(1,5\text{-COD})Cl]_2$ (250 mg, 0.372 mmol) was dissolved in 6 mL of DCM in a 20 mL scintillation vial, forming an orange solution. After 5 min of stirring, 1.5 mL of CH_3CN was added to the solution, which quickly turned yellow. The solution was stirred for 5 min to ensure all components were fully dissolved, and then $AgBF_4$ (150 mg, 0.771 mmol) was added, immediately forming a white-gray precipitate of AgCl. The reaction mixture was stirred for 10 min and then filtered through a glass frit to remove AgCl. An additional ca. 5 mL of DCM was used to rinse the vial and frit. To the yellow filtrate was added ∼50 mL of diethyl ether, which caused the instantaneous precipitation of fine yellow crystals of $[Ir(1,5\text{-COD})(CH_3CN)_2](BF_4)$. The crystals were collected under vacuum on a 15 mL glass frit, washed with two 15 mL aliquots of ether, and left for 5 min to dry. The crystals were transferred to a 20 mL scintillation vial and dried under vacuum overnight (286 mg, 0.609 mmol, 81.8% yield). ^{1}H NMR (400 MHz, $CDCl_3$): δ 1.72 (m, CH2), 2.26 (m, CH2), 2.57 (s, CH3), 4.22 (s, br, CH). ^{13}C NMR (101 MHz, $CDCl_3$): δ 3.50, 31.27, 70.68, 123.19.

Pt(CH$_3$CN)$_2$Cl$_2$. $PtCl_2(CH_3CN)_2$ was prepared from $PtCl_2$ following a slightly modified literature procedure.[44] Under an N_2 atmosphere, $PtCl_2$ (199 mg, 0.748 mmol) was suspended in 25 mL of CH_3CN in a 100 mL Schlenk flask. A magnetic stir bar was added, and the reaction mixture was stirred and heated to reflux overnight, during which the $PtCl_2$ fully dissolved to give a pale-yellow solution. The solution was allowed to cool to room temperature and then concentrated in vacuo to ca. 10 mL in volume, precipitating yellow solids. Under air, the solids were recovered on a 15 mL glass frit, washed with two 15 mL aliquots of hexanes, and dried overnight under vacuum (203 mg, 0.583 mmol, 78% yield).

[Pt(CH$_3$CN)$_4$](BF$_4$)$_2$. The Pt(II) metalation complex $[Pt(CH_3CN)_4](BF_4)_2$ was prepared with a slight modification of the reported procedure.[45] In a N_2 glovebox, a 100 mL Schlenk flask was charged with $AgBF_4$ (230. mg, 1.18 mmol), 20 mL of dry CH_3CN, and a magnetic stir bar. The flask was transferred to a Schlenk line, and $PtCl_2(CH_3CN)_2$ (203 mg, 0.583 mmol) was added under positive pressure of N_2. The hood light was shut off, the flask was wrapped in Al foil to mitigate photodegradation of $AgBF_4$, and the reaction mixture was heated to reflux for 4 h under N_2. The reaction mixture was then allowed to cool to room temperature and the foil removed, revealing a yellow solution with a white-gray precipitate of AgCl. Under air, the solution was filtered over a Celite pad to remove AgCl, and the yellow filtrate was concentrated in vacuo to ca. 5 mL. A 50 mL portion of ether was poured into the flask, which caused the instantaneous precipitation of fine white crystals of $[Pt(CH_3CN)_4](BF_4)_2$. The product was collected on a 15 mL glass frit, washed with two 10 mL portions of ether, and dried overnight under vacuum. The final product was then transferred to a 20 mL scintillation vial and stored under a N_2 atmosphere (169 mg, 0.317 mmol, 54.4% yield). ^{1}H NMR (400 MHz, CD_3CN): δ 2.61 (s, CH_3). ^{13}C NMR (101 MHz, CD_3CN): δ 4.41.

General Method for Postsynthetic Metalation of Zr-TpmC.* In an N_2-filled glovebox, 100 mg of activated Zr-TpmC* was charged into a 20 mL vial. A PGM metalation complex (1.0 equiv/TpmC* site) was dissolved in CH_3CN (10 mL) and added into the vial containing Zr-TpmC*. The vial was capped and left undisturbed for 1 week. The metalation solution was decanted and the MOF soaked in 20 mL of fresh CH_3CN overnight to remove unbound metal complex. The supernatant was decanted and replaced with fresh CH_3CN every 24 h, and the MOF was soaked in fresh CH_3CN for 3 days. The MOF was then soaked in fresh DCM following the same soaking procedure for 3 days. The MOF was then activated at room temperature under dynamic vacuum overnight to give a microcrystalline powder.

Metalation of Zr-TpmC by [Pd(CH$_3$CN)$_4$](BF$_4$)$_2$ to Produce Pd(CH$_3$CN)$_2$(BF$_4$)$_2$@Zr-TpmC* (1).* The preparation followed the generic procedure, using 100 mg of MOF (0.0171 mmol) and 64.6 mg of $[Pd(CH_3CN)_4](BF_4)_2$ (0.145 mmol). Elemental analysis: Pd:Zr = 0.378:1.000, as determined by ICP-MS.

Metalation of Zr-TpmC by [RhCl(CO)$_2$]$_2$ to Produce RhCl(CO)$_2$@Zr-TpmC* (2).* The preparation followed the generic procedure, using 50 mg of MOF (8.5 μmol) and 13.3 mg of $[RhCl(CO)_2]_2$ (0.0342 mmol). Elemental analysis: Rh:Zr = 0.184:1, as determined by ICP-MS.

Metalation of Zr-TpmC by [Ir(1,5-COD)(CH$_3$CN)$_2$]BF$_4$ to Produce Ir(1,5-COD)BF$_4$@Zr-TpmC*(3).* The preparation followed the generic procedure, using 100 mg of MOF (0.0171 mmol) and 69 mg of $[Ir(1,5\text{-COD})(CH_3CN)_2](BF_4)$ (0.15 mmol). Elemental analysis: Ir:Zr = 0.020:1.000, as determined by ICP-MS.

https://doi.org/10.1021/acs.inorgchem.1c00941
Inorg. Chem. XXXX, XXX, XXX−XXX

Metalation of Zr-TpmC by $[Pt(CH_3CN)_4](BF_4)_2$ to Produce $Pt(CH_3CN)_2(BF_4)_2$@Zr-TpmC* (4).* The preparation followed the generic procedure, using 100 mg of Zr-TpmC* (0.0171 mmol) and 78 mg of $[Pt(CH_3CN)_4](BF_4)_2$ for the metalation solution. Elemental analysis: Pt:Zr = 0.023:1.000, as determined by ICP-MS.

Direct Synthesis of $IrCl_3$@Zr-TpmC (**5**).* In a 100 mL glass bottle, 344. mg of iridium(III) chloride hydrate (0.966 mmol, 1.28 equiv) and 324. mg of TpmC* (0.753 mmol, 1.00 equiv) were dissolved in 10 mL of DMF and stirred for 1 h, forming a deep-red/purple solution. In a separate 100 mL Erlenmeyer flask, 555 mg of $ZrOCl_2 \cdot 8H_2O$ (1.72 mmol, 2.28 equiv) and 14.7 g of benzoic acid (120 mmol, 159 equiv) were sonicated in 50 mL of DMF until dissolved to form a colorless solution. The contents of the Erlenmeyer flask was then transferred to the glass bottle containing Ir and TpmC*, which was then tightly capped and heated to 120 °C for 4.5 days. After cooling to room temperature, the yellow supernatant was decanted and the remaining white solids were transferred to a 20 mL scintillation vial. The solids were then washed with three 20 mL portions of DMF, soaking in each wash for at least 1 h, followed by two 20 mL portions of acetone, again soaking for at least 1 h. The white solids were then activated overnight at 110 °C under high vacuum to yield **5**. Yield: 258 mg of activated MOF. Elemental analysis: Ir:Zr = 0.395:1.000, as determined by ICP-MS.

Direct Synthesis of $RhCl_3$@Zr-TpmC (**6**).* In a 20 mL scintillation vial, 37 mg of rhodium(III) chloride hydrate (0.14 mmol, 1.0 equiv) and 62 mg of TpmC* (0.14 mmol, 1.0 equiv) were dissolved in 3 mL of 1:1 DMF/H_2O to form a deep-red solution. In a separate 20 mL scintillation vial, 82 mg of $ZrOCl_2 \cdot 8H_2O$ (0.25 mmol, 1.8 equiv) and 2.5 g of benzoic acid (20 mmol, 140 equiv) were sonicated in 3 mL of DMF until dissolved to form a colorless solution. The two solutions were then combined in one vial, which was capped and heated to 60 °C for 24 h. After cooling to room temperature, the gray-green solids were collected by centrifugation and washed with three 20 mL portions of DMF, soaking in each wash for at least 1 h, followed by two 20 mL portions of acetone, again soaking for at least 1 h. Yield: 148 mg of unactivated MOF. Elemental analysis: Rh:Zr = 0.166:1.000, as determined by ICP-MS.

Direct Synthesis of K_2PtCl_6@Zr-TpmC.* In a 20 mL scintillation vial, 24.2 mg of potassium hexachloroplatinate (0.0498 mmol, 1.00 equiv) and 22.0 mg of TpmC* (0.0511 mmol, 1.03 equiv) were dissolved in 3 mL of 1:1 DMF/H_2O to form a yellow solution. In a separate 20 mL scintillation vial, 41.3 mg of $ZrOCl_2 \cdot 8H_2O$ (0.128 mmol, 2.50 equiv) and 1.09 g of benzoic acid (8.93 mmol, 175 equiv) were sonicated in 2 mL of DMF until dissolved to form a colorless solution. The two solutions were then combined in one vial, which was capped and heated to 60 °C for 24 h. After cooling to room temperature, the gray solids were collected by centrifugation and washed with three 20 mL portions of DMF, soaking in each wash for at least 1 h, followed by two 20 mL portions of acetone, again soaking for at least 1 h. Yield: 44.1 mg of unactivated MOF. Elemental analysis: Pt:Zr = 0.063:1.000, as determined by ICP-MS.

Computational Methods. Computational work was performed using the facilities provided by the Massachusetts Green High Performance Computing Center. All calculations were performed with the *Gaussian 03*[46] program package. Geometry optimization was carried out with the M06 density functional,[47] using the 6-311G(d,p) basis set[48] for all nonmetal atoms and the SDD basis set[49] for the Pd atom. The M06 functional was chosen for its enhanced description of the dispersion effects. The model structure for optimization by DFT is a truncated cluster model of the formula $[Pd(CH_3CN)_2(TpmC^*)]^{2+}$ (Figure S38). The starting geometry of TpmC* was based on the crystallographic data for Zr-TpmC*,[18] and the geometry of Pd^{2+} was assumed to be square-planar based on the crystallographic data for $[Pd(Tpm)_2](BF_4)_2$ and $[Pd(CH_3CN)_4](BF_4)_2$.[24,28] Structures were allowed to fully optimize such that no imaginary frequencies were observed. The structural rigidity, imparted on TpmC* by the extended structure of the MOF, was modeled by constraining the position of the C and O atoms in the three terminal carboxyls of TpmC* during geometry optimization.

■ ASSOCIATED CONTENT

Supporting Information

The Supporting Information is available free of charge at https://pubs.acs.org/doi/10.1021/acs.inorgchem.1c00941.

NMR data, further PXRD characterization data, XANES results, experimental details and results on Rh and Pd loading screens, surface area measurements, XPS results, DFT-assisted EXAFS fitting parameters and data, and synthetic schemes (PDF)

■ AUTHOR INFORMATION

Corresponding Author

Mircea Dincă − *Department of Chemistry, Massachusetts Institute of Technology (MIT), Cambridge, Massachusetts 02139, United States;* orcid.org/0000-0002-1262-1264; Phone: (617) 253-4154; Email: mdinca@mit.edu

Authors

Michael T. Payne − *Department of Chemistry, Massachusetts Institute of Technology (MIT), Cambridge, Massachusetts 02139, United States*

Constanze N. Neumann − *Department of Chemistry, Massachusetts Institute of Technology (MIT), Cambridge, Massachusetts 02139, United States;* Present Address: Department of Heterogeneous Catalysis, Max-Planck Institut für Kohlenforschung, Kaiser-Wilhelmplatz 1, 45470 Muelheim, Germany; orcid.org/0000-0003-1004-1140

Eli Stavitski − *National Synchrotron Light Source II (NSLS-II), Brookhaven National Laboratory (BNL), Upton, New York 11973, United States*

Complete contact information is available at: https://pubs.acs.org/10.1021/acs.inorgchem.1c00941

Author Contributions

The manuscript was written through contributions of all authors. All authors have given approval to the final version of the manuscript.

Funding

This work was supported by funding from the Dow Chemical Company.

Notes

The authors declare no competing financial interest.

■ ACKNOWLEDGMENTS

This research used beamline 8-ID (ISS) of the NSLS-II, a U.S. Department of Energy (DOE), Office of Science User Facility, operated for the DOE Office of Science by BNL under Contract DE-SC0012704. We thank Dr. Joo Kang at the Dow Chemical Company for assistance with XPS measurements, and Dr. Steve Rozeveld at the Dow Chemical Company for assistance with TEM/EDS measurements. We thank Dr. James Bour for assistance with DFT calculations, and Dr. Amanda Stubbs for assistance with XAS measurements. We also thank Dr. Chenyue Sun for providing ligand and MOF samples and for scientific discussions.

■ REFERENCES

(1) Trofimenko, S. Boron-Pyrazole Chemistry. II. Poly(1-Pyrazolyl)-Borates. *J. Am. Chem. Soc.* **1967**, *89* (13), 3170−3177.

(2) Byers, P. K.; Canty, A. J.; Honeyman, R. T. Organometallic Chemistry of Palladium and Platinum with Poly(Pyrazol-1-Yl)Alkanes

and Poly(Pyrazol-1-Yl)Borates. *Adv. Organomet. Chem.* **1992**, *34*, 1–65.
(3) Slugovc, C.; Padilla-Martínez, I.; Sirol, S.; Carmona, E. Rhodium- and Iridium-Trispyrazolylborate Complexes C H Activation and Coordination Chemistry. *Coord. Chem. Rev.* **2001**, *213*, 129–157.
(4) Calabrese, J. C.; Trofimenko, S.; Thompson, J. S. A New Class of Polypyrazolylborate Ligands. *J. Chem. Soc., Chem. Commun.* **1986**, *17* (14), 1122.
(5) Furukawa, H.; Cordova, K. E.; O'Keeffe, M.; Yaghi, O. M. The Chemistry and Applications of Metal-Organic Frameworks. *Science (Washington, DC, U. S.)* **2013**, *341* (6149), 1230444.
(6) Brozek, C. K.; Dincă, M. Thermodynamic Parameters of Cation Exchange in MOF-5 and MFU-4l. *Chem. Commun.* **2015**, *51* (59), 11780–11782.
(7) Metzger, E. D.; Brozek, C. K.; Comito, R. J.; Dinca, M. Selective Dimerization of Ethylene to 1-Butene with a Porous Catalyst. *ACS Cent. Sci.* **2016**, *2* (3), 148–153.
(8) Comito, R. J.; Metzger, E. D.; Wu, Z.; Zhang, G.; Hendon, C. H.; Miller, J. T.; Dincă, M. Selective Dimerization of Propylene with Ni-MFU-4l. *Organometallics* **2017**, *36* (9), 1681–1683.
(9) Comito, R. J.; Wu, Z.; Zhang, G.; Lawrence, J. A.; Korzyński, M. D.; Kehl, J. A.; Miller, J. T.; Dincă, M. Stabilized Vanadium Catalyst for Olefin Polymerization by Site Isolation in a Metal–Organic Framework. *Angew. Chem., Int. Ed.* **2018**, *57* (27), 8135–8139.
(10) Denysenko, D.; Jelic, J.; Reuter, K.; Volkmer, D. Postsynthetic Metal and Ligand Exchange in MFU-4l: A Screening Approach toward Functional Metal-Organic Frameworks Comprising Single-Site Active Centers. *Chem. - Eur. J.* **2015**, *21* (22), 8188–8199.
(11) Denysenko, D.; Grzywa, M.; Jelic, J.; Reuter, K.; Volkmer, D. Scorpionate-Type Coordination in MFU-4l Metal-Organic Frameworks: Small-Molecule Binding and Activation upon the Thermally Activated Formation of Open Metal Sites. *Angew. Chem., Int. Ed.* **2014**, *53* (23), 5832–5836.
(12) Stubbs, A. W.; Dincă, M. Selective Oxidation of C–H Bonds through a Manganese(III) Hydroperoxo in Mn II -Exchanged CFA-1. *Inorg. Chem.* **2019**, *58* (19), 13221–13228.
(13) Wang, C.-H.; Gao, W.-Y.; Ma, Q.; Powers, D. C. Templating Metastable Pd 2 Carboxylate Aggregates. *Chem. Sci.* **2019**, *10* (6), 1823–1830.
(14) Tu, W.; Xu, Y.; Yin, S.; Xu, R. Rational Design of Catalytic Centers in Crystalline Frameworks. *Adv. Mater.* **2018**, *30* (33), 1707582.
(15) Drake, T.; Ji, P.; Lin, W. Site Isolation in Metal-Organic Frameworks Enables Novel Transition Metal Catalysis. *Acc. Chem. Res.* **2018**, *51* (9), 2129–2138.
(16) Dhakshinamoorthy, A.; Li, Z.; Garcia, H. Catalysis and Photocatalysis by Metal Organic Frameworks. *Chem. Soc. Rev.* **2018**, *47*, 8134.
(17) Drake, T.; Ji, P.; Lin, W. Site Isolation in Metal-Organic Frameworks Enables Novel Transition Metal Catalysis. *Acc. Chem. Res.* **2018**, *51* (9), 2129–2138.
(18) Sun, C.; Skorupskii, G.; Dou, J.-H.; Wright, A. M.; Dincă, M. Reversible Metalation and Catalysis with a Scorpionate-like Metallo-Ligand in a Metal–Organic Framework. *J. Am. Chem. Soc.* **2018**, *140* (50), 17394–17398.
(19) Khusnutdinova, J. R.; Rath, N. P.; Mirica, L. M. The Conformational Flexibility of the Tetradentate Ligand TBu N4 Is Essential for the Stabilization of (TBu N4)Pd III Complexes. *Inorg. Chem.* **2014**, *53* (24), 13112–13129.
(20) Qu, F.; Khusnutdinova, J. R.; Rath, N. P.; Mirica, L. M. Dioxygen Activation by an Organometallic Pd(II) Precursor: Formation of a Pd(IV)-OH Complex and Its C-O Bond Formation Reactivity. *Chem. Commun.* **2014**, *50* (23), 3036–3039.
(21) Krieble, V. K.; Noll, C. I. The Hydrolysis of Nitriles with Acids. *J. Am. Chem. Soc.* **1939**, *61* (3), 560–563.
(22) Canty, A. J.; Hoare, J. L.; Skelton, B. W.; White, A. H.; Van Koten, G. Synthesis and Reactivity of Poly(Pyrazol-1-Yl)Borate Derivatives of Cyclopalladation Systems, Including Structural Studies of Pd{2-CH2C6H4P(o-Tolyl)2-C,P}{(Pz)3BH-N,N′} and Pd-(C6H4C5H4N-C2,N′){(Pz)3BH-N,N′}. *J. Organomet. Chem.* **1998**, *552* (1–2), 23–29.
(23) Korzyński, M. D.; Braglia, L.; Borfecchia, E.; Lamberti, C.; Dinca, M. Molecular Niobium Precursors in Various Oxidation States: An XAS Case Study. *Inorg. Chem.* **2018**, *57*, 13998.
(24) Edwards, P. G.; Paisey, S. J.; Albers, T. CCDC 101970: Experimental Crystal Structure Determination. *CDC Commun.* **1999**.
(25) Maihom, T.; Wannakao, S.; Boekfa, B.; Limtrakul, J. Production of Formic Acid via Hydrogenation of CO2 over a Copper-Alkoxide-Functionalized MOF: A Mechanistic Study. *J. Phys. Chem. C* **2013**, *117* (34), 17650–17658.
(26) Odoh, S. O.; Cramer, C. J.; Truhlar, D. G.; Gagliardi, L. Quantum-Chemical Characterization of the Properties and Reactivities of Metal-Organic Frameworks. *Chem. Rev.* **2015**, *115* (12), 6051–6111.
(27) Ortuño, M. A.; Bernales, V.; Gagliardi, L.; Cramer, C. J. Computational Study of First-Row Transition Metals Supported on MOF NU-1000 for Catalytic Acceptorless Alcohol Dehydrogenation. *J. Phys. Chem. C* **2016**, *120* (43), 24697–24705.
(28) Canty, A. J.; Minchin, N. J.; Engelhardt, L. M.; Skelton, B. W.; White, A. H. Interaction of Palladium(II) with Polydentate Ligands, Including the Synthesis and Structure of Bis[Tris(Pyrazol-1-Yl)-Borato-N,N′]Palladium(II) and the Cations [Pd(L)2]2+ [L = Tris(Pyrazol-1-Yl)Methane-N,N′ or Tris(Pyridin-2-Yl)Methane-N,N′]. *J. Chem. Soc., Dalton Trans.* **1986**, *0* (3), 645–650.
(29) Brock, C. P.; Das, M. K.; Minton, R. P.; Niedenzu, K. Pyrazole Derivatives of Diborane(4). *J. Am. Chem. Soc.* **1988**, *110* (3), 817–822.
(30) Mlateček, M.; Dostál, L.; Růžičková, Z.; Honzíček, J.; Holubová, J.; Erben, M. The First Scorpionate Ligand Based on Diazaphosphole. *Dalt. Trans.* **2015**, *44* (46), 20242–20253.
(31) Hickman, A. J.; Sanford, M. S. High-Valent Organometallic Copper and Palladium in Catalysis. *Nature*; Nature Publishing Group, April 11, 2012; pp 177–185; DOI: 10.1038/nature11008.
(32) Sehnal, P.; Taylor, R. J. K.; Fairlamb, I. J. S. Emergence of Palladium(IV) Chemistry in Synthesis and Catalysis. *Chem. Rev.* **2010**, *110* (2), 824–889.
(33) Shi, W.; Zeng, L.; Cao, L.; Huang, Y.; Wang, C.; Lin, W. Metal-Organic Layers as Reusable Solid Fluorination Reagents and Heterogeneous Catalysts for Aromatic Fluorination. *Nano Res.* **2021**, *14* (2), 473–478.
(34) Purwoko, A. A.; Lees, A. J. Photochemical C-H Bond Activation Reactivity of (HBPz' 3)Rh(CO) 2 (Pz' = 3,5-Dimethylpyrazolyl) in Alkane Solutions. *Inorg. Chem.* **1996**, *35* (3), 675–682.
(35) Ghosh, C. K.; Graham, W. A. G. Efficient and Selective Carbon-Hydrogen Activation by a Tris(Pyrazolylborate)Rhodium Complex. *J. Am. Chem. Soc.* **1987**, *109* (15), 4726–4727.
(36) Øien-ØDegaard, S.; Shearer, G. C.; Wragg, D. S.; Lillerud, K. P. Pitfalls in Metal-Organic Framework Crystallography: Towards More Accurate Crystal Structures. *Chem. Soc. Rev.* **2017**, *46* (16), 4867–4876.
(37) Sizova, O. V.; Varshavskii, Y. S.; Nikol'skii, A. B. Binuclear Rhodium(I) Carbonyl Carboxylate Complexes: DFT Study of Structural and Spectral Properties. *Russ. J. Coord. Chem.* **2005**, *31* (12), 875–883.
(38) Jung, J. C.; Watkins, E. B.; Avery, M. A. Synthesis of 3-Substituted and 3,4-Disubstituted Pyrazolin-5-Ones. *Tetrahedron* **2002**, *58* (18), 3639–3646.
(39) Brunauer, S.; Emmett, P. H.; Teller, E. Adsorption of Gases in Multimolecular Layers. *J. Am. Chem. Soc.* **1938**, *60* (2), 309–319.
(40) Rouquerol, J.; Llewellyn, P.; Rouquerol, F. Is the BET Equation Applicable to Microporous Adsorbents? *Stud. Surf. Sci. Catal.* **2007**, *160*, 49–56.
(41) Ravel, B.; Newville, M. ATHENA, ARTEMIS, HEPHAESTUS: Data Analysis for X-Ray Absorption Spectroscopy Using IFEFFIT. *J. Synchrotron Radiat.* **2005**, *12* (4), 537–541.

https://doi.org/10.1021/acs.inorgchem.1c00941
Inorg. Chem. XXXX, XXX, XXX–XXX

(42) Newville, M. IFEFFIT: Interactive XAFS Analysis and FEFF Fitting. *J. Synchrotron Radiat.* **2001**, *8* (2), 322−324.
(43) Whitehead, C. B.; Finke, R. G. Nucleation Kinetics and Molecular Mechanism in Transition-Metal Nanoparticle Formation: The Intriguing, Informative Case of a Bimetallic Precursor, {[(1,5-COD)Ir I ·HPO 4] 2 } 2-. *Chem. Mater.* **2019**, *31* (8), 2848−2862.
(44) Fraccarollo, D.; Bertani, R.; Mozzon, M.; Belluco, U.; Michelin, R. A. Synthesis and Spectroscopic Investigation of Cis and Trans Isomers of Bis(Nitrile)Dichloroplatinum(II) Complexes. *Inorg. Chim. Acta* **1992**, *201* (1), 15−22.
(45) Muller, T. E.; Green, J. C.; Mingos, D. M. P.; Mcpartlin, C. M.; Whittingham, C.; Williams, D. J.; Woodroffe, T. M. Complexes of Gold(I) and Platinum (II) with Polyaromatic Phosphine. *J. Organomet. Chem.* **1998**, *551*, 313.
(46) Frisch, M. J.; Trucks, G. W.; Schlegel, H. B.; Scuseria, G. E.; Robb, M. A.; Cheeseman, J. R.; Montgomery, J. A., Jr.; Vreven, T.; Kudin, K. N.; Burant, J. C.; Millam, J. M.; Iyengar, S. S.; Tomasi, J.; Barone, V.; Mennucci, B.; Cossi, M.; Scalmani, G.; Rega, N.; Petersson, G. A.; Nakatsuji, H.; Hada, M.; Ehara, M.; Toyota, K.; Fukuda, R.; Hasegawa, J.; Ishida, M.; Nakajima, T.; Honda, Y.; Kitao, O.; Nakai, H.; Klene, M.; Li, X.; Knox, J. E.; Hratchian, H. P.; Cross, J. B.; Bakken, V.; Adamo, C.; Jaramillo, J.; Gomperts, R.; Stratmann, R. E.; Yazyev, O.; Austin, A. J.; Cammi, R.; Pomelli, C.; Ochterski, J. W.; Ayala, P. Y.; Morokuma, K.; Voth, G. A.; Salvador, P.; Dannenberg, J. J.; Zakrzewski, V. G.; Dapprich, S.; Daniels, A. D.; Strain, M. C.; Farkas, O.; Malick, D. K.; Rabuck, A. D.; Raghavachari, K.; Foresman, J. B.; Ortiz, J. V.; Cui, Q.; Baboul, A. G.; Clifford, S.; Cioslowski, J.; Stefanov, B. B.; Liu, G.; Liashenko, A.; Piskorz, P.; Komaromi, I.; Martin, R. L.; Fox, D. J.; Keith, T.; Al-Laham, M. A.; Peng, C. Y.; Nanayakkara, A.; Challacombe, M.; Gill, P. M. W.; Johnson, B.; Chen, W.; Wong, M. W.; Gonzalez, C.; Pople, J. A. *Gaussian 03*; Gaussian Inc.: Wallingford, CT, 2004.
(47) Zhao, Y.; Truhlar, D. G. The M06 Suite of Density Functionals for Main Group Thermochemistry, Thermochemical Kinetics, Noncovalent Interactions, Excited States, and Transition Elements: Two New Functionals and Systematic Testing of Four M06-Class Functionals and 12 Other Function. *Theor. Chem. Acc.* **2008**, *120* (1−3), 215−241.
(48) Krishnan, R.; Binkley, J. S.; Seeger, R.; Pople, J. A. Self-Consistent Molecular Orbital Methods. XX. A Basis Set for Correlated Wave Functions. *J. Chem. Phys.* **1980**, *72* (1), 650−654.
(49) Andrae, D.; Häußermann, U.; Dolg, M.; Stoll, H.; Preuß, H. Energy-Adjusted Ab Initio Pseudopotentials for the Second and Third Row Transition Elements. *Theor. Chim. Acta* **1990**, *77* (2), 123−141.

https://doi.org/10.1021/acs.inorgchem.1c00941
Inorg. Chem. XXXX, XXX, XXX−XXX